

## Andrew Honeycutt

Department of Mechanical Engineering and  
Engineering Science,  
University of North Carolina at Charlotte,  
9201 University City Boulevard,  
Charlotte, NC 28223  
e-mail: ahoney15@uncc.edu

## Tony L. Schmitz<sup>1</sup>

Mem. ASME  
Department of Mechanical Engineering and  
Engineering Science,  
University of North Carolina at Charlotte,  
9201 University City Boulevard,  
Charlotte, NC 28223  
e-mail: tony.schmitz@uncc.edu

# Milling Stability Interrogation by Subharmonic Sampling

*This paper describes the use of subharmonic sampling to distinguish between different instability types in milling. It is demonstrated that sampling time-domain milling signals at integer multiples of the tooth period enables secondary Hopf and period- $n$  bifurcations to be automatically differentiated. A numerical metric is applied, where the normalized sum of the absolute values of the differences between successively sampled points is used to distinguish between the potential bifurcation types. A new stability map that individually identifies stable and individual bifurcation zones is presented. The map is constructed using time-domain simulation and the new subharmonic sampling metric.*  
[DOI: 10.1115/1.4034894]

**Keywords:** machining, stability, bifurcation, periodic, sampling

## Introduction

Machining stability may be analyzed by numerical, analytical, or semi-analytical solutions of the second-order delay differential equations that describe the system dynamic behavior. It has been demonstrated by many researchers that stable and unstable ( chatter) cutting conditions may be predicted based on the selected operating parameters, typically spindle speed and chip width. In a recent study, a new metric was described that automatically differentiates between stable and unstable behavior for time-domain simulation of the milling processes [1]. The approach is based on periodic sampling of milling signals at once per tooth period,  $\tau$ . In this paper, the technique will be extended to include subharmonic sampling at  $n\tau$  ( $n=2, 3, 4, \dots$ ) to automatically distinguish between the various types of instability, including secondary (subcritical) Hopf, or Neimark-Sacker, and period- $n$  bifurcations<sup>2</sup> ( $n=2, 3, 4, \dots$ ). This paper is organized as follows: First, background information on milling stability prediction, with an emphasis on period- $n$  bifurcations, is provided. Second, the application of subharmonic sampling to time-domain milling simulation results and the subsequent identification of period- $n$  bifurcations are demonstrated. Third, a new stability map based on subharmonic sampling is presented. Finally, conclusions are presented.

## Background

During the mid-19th century, self-excited vibrations were first described using time-delay differential equations [2,3]. The feed-back mechanism (time-delay term) was defined as “regeneration of waviness,” where the previously cut surface combined with the instantaneous vibration state dictates the current chip thickness, force level, and corresponding vibration response [4–7]. This work resulted in analytical algorithms that were used to produce the now well-known stability lobe diagram that separates the spindle speed-chip width domain into regions of stable and unstable behavior [6–18].

**Period- $n$  Bifurcations.** In 1998, Davies et al. used once per revolution sampling to characterize the synchronicity of cutting tool motions with the tool rotation in milling [19]. They observed the traditional secondary Hopf bifurcation [20], as well as period-3 tool motion (i.e., motion that repeated with a period of three cutter revolutions) during partial radial immersion milling. In 2000,

Davies et al. further examined the stability of highly interrupted machining [21] by developing a two-stage map to describe: (1) noncutting motions governed by an analytical solution and (2) motions during cutting using an approximation (fixed tool position with a change in momentum). They reported a doubling of the number of optimally stable spindle speeds when the time in cut is small. Experiments confirmed the new, low radial immersion best speeds.

In 2001, Moon and Kalmár-Nagy reviewed the “prediction of complex, unsteady, and chaotic dynamics” in machining [20]. They listed the various contributors to nonlinear behavior, including the loss of tool-workpiece contact due to large amplitude vibration and workpiece material constitutive relations and highlighted previous applications of nonlinear dynamics methods to the study of chatter [22–27]. They also specified the use of phase-space methods, such as Poincaré maps, to identify changes in machining process dynamics.

Time-domain simulation has been used extensively to study milling behavior [28,29]. For example, Zhao and Balachandran implemented time-domain simulation, which incorporated loss of tool-workpiece contact and regeneration, to study the process dynamics [30]. They identified secondary Hopf bifurcation and suggested that “period-doubling bifurcations are believed to occur” for low radial immersions. They included bifurcation diagrams for limited axial depth of cut ranges at two spindle speeds to demonstrate the two bifurcation types.

Davies et al. extended their initial work in 2002 to present the first analytical stability boundary for highly interrupted machining [31]. It was based on modeling the cutting process as a kicked harmonic oscillator with a time delay and followed the two-stage map concept described in Ref. [21]. They used the frequency content of a microphone signal to establish the existence of both secondary Hopf and period-2 (or period-doubling or flip) instabilities. Mann et al. also provided experimental validation of secondary Hopf and period-2 instabilities for up and down milling [32]. They reported “a kind of period triple phenomenon” observed using the once per revolution sampled displacement signal recorded from a single degree-of-freedom flexure-based machining platform.

The semidiscretization, time finite-element analysis, and multi-frequency methods were also developed to produce milling stability charts that predict both instabilities [33–37]. In Ref. [38], it was shown using the semidiscretization method that the period-2 bifurcation exhibits closed curves within the secondary Hopf lobes, except for the highest speed stability lobe. Simultaneous secondary Hopf (quasi-periodic) and period-2 bifurcation behaviors were also observed. It was reported that this “combination” behavior occurred at unstable axial depths of cut above the period-2 lobes. Additionally, period-3 instability was seen and it

<sup>1</sup>Corresponding author.

<sup>2</sup>A general definition for bifurcation is a dramatic change in the system state or behavior.

Manuscript received May 24, 2016; final manuscript received September 16, 2016; published online October 19, 2016. Assoc. Editor: Laine Mears.

was noted that this “periodic chatter” with period-3 (or higher) always occurred above a secondary Hopf stability limit. The same group [39] reported further experimental evidence of secondary Hopf, period-2, -3, -4, and combined secondary Hopf, and period-2 chatter, depending on the spindle speed-axial depth values for a two degree-of-freedom dynamic system. A perturbation analysis was performed in Ref. [40] to identify the secondary Hopf and period-2 instabilities. Additionally, numerical integration was implemented to construct a bifurcation diagram for a selected spindle speed that demonstrated the transition from stable operation to quasi-periodic chatter as the axial depth is increased. Stépán et al. continued to explore the nonlinear aspects of milling behavior in 2005 [41]. They described stable period-2 motion where the tool does not contact the workpiece in each tooth period (even in the absence of runout). For a two flute cutter, for example, only one tooth contacts the workpiece per revolution; they referred to this condition as the “fly over effect” and included a bifurcation diagram for these proposed stable and unstable period-2 oscillations.

The effect of the helix angle on period-2 instability was first studied by Zatarain et al. [42]. They found that, depending on the helix angle, the closed curves within the secondary Hopf lobes change their size and shape. They also found that these closed islands of stability can appear even in the highest speed stability lobe (in contrast to the results when helix angle is not considered). This work was continued in Ref. [43], where the authors showed that at axial depths equal to the axial pitch of the cutter teeth, the equation of motion becomes an autonomous delay differential equation, so the period-2 instability is not possible. Patel et al. studied the helix effect in up and down milling using the time finite-element approach in Ref. [44].

In recent work, Moradi et al. included tool wear and process damping in the bifurcation analysis of milling behavior [45]. Also, Honeycutt and Schmitz presented “extended milling bifurcation diagrams” that revealed higher order period- $n$  bifurcations at depths of cut well above the traditional stability limit [46]. Period-2, -3, -6, -7, -8, and -15 bifurcations were predicted and experimentally validated for milling in Ref. [47]. The sensitivity of period- $n$  bifurcation behavior to the structural dynamics (natural frequency and damping) was studied both numerically and experimentally.

## Subharmonic Sampling

In this section, the time-domain milling simulation algorithm implemented in this study is first described. The periodic sampling metric is then reviewed. Finally, subharmonic sampling for the differentiation of bifurcation types is demonstrated.

**Time-Domain Simulation.** Time-domain simulation enables the numerical solution of the coupled, time-delay equations of motion for milling in small time steps [48]. It is well-suited for incorporating all the intricacies of milling dynamics, including the nonlinearity that occurs if the tooth leaves the cut due to large amplitude vibrations and complicated tool geometries (including runout, or different radii, of the cutter teeth, nonproportional teeth spacing, and variable helix). The simulation is based on the regenerative force, dynamic deflection model described by Smith and Tlustý [28]. As opposed to stability maps that provide a global picture of the stability behavior, time-domain simulation provides information regarding the local cutting force and vibration behavior for the selected cutting conditions. The simulation used in this study proceeds as follows (see Fig. 1):

- (1) The instantaneous chip thickness,  $h(t)$ , is determined using the vibration of the current and previous teeth at the selected tooth angle.
- (2) The cutting force components in the tangential ( $t$ ) and normal ( $n$ ) directions are calculated using

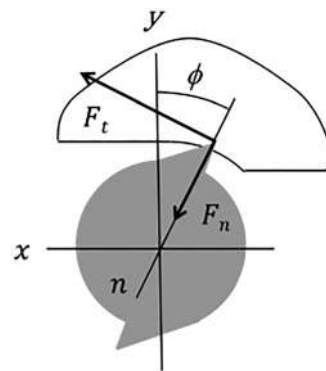


**Fig. 1 Cutting force geometry.** The normal and tangential direction cutting forces,  $F_n$  and  $F_t$ , are identified. The fixed  $x$  and  $y$  directions, as well as the rotating normal direction,  $n$ , are also shown. The angle  $\phi$  defines the tooth angle. The tool feed is to the right for the clockwise tool rotation, and the axial depth is in the  $z$  direction.

$$\begin{aligned} F_t(t) &= k_{tc}bh(t) + k_{te}b \\ F_n(t) &= k_{nc}bh(t) + k_{ne}b \end{aligned} \quad (1)$$

where  $b$  is the axial depth of cut, and the cutting force coefficients are identified by the subscripts  $t$  or  $n$  for direction and  $c$  or  $e$  for cutting or edge effect.

- (3) The force components are used to find the new displacements by numerical solution of the differential equations of motion in the  $x$  and  $y$  directions

$$\begin{aligned} m_x\ddot{x} + c_x\dot{x} + k_x x &= F_t(t)\cos(\phi) + F_n\sin(\phi) \\ m_y\ddot{y} + c_y\dot{y} + k_y y &= F_t(t)\sin(\phi) - F_n\cos(\phi) \end{aligned} \quad (2)$$

where  $m$  is the modal mass,  $c$  is the modal viscous damping coefficient, and  $k$  is the modal stiffness. The subscripts identify the direction and multiple degrees-of-freedom in each direction can be accommodated.

- (4) The tool rotation angle is incremented, and the process is repeated.

The instantaneous chip thickness depends on the nominal, tooth angle-dependent chip thickness, the current vibration in the direction normal to the surface, and the vibration of previous teeth at the same angle. The chip thickness can be expressed using the circular tooth path approximation as

$$h(t) = f_i \sin(\phi) + n(t - \tau) - n(t) \quad (3)$$

where  $f_i$  is the commanded feed per tooth,  $\phi$  is the tooth angle,  $n$  is the normal direction (see Fig. 1), and  $\tau$  is the tooth period. The tooth period is defined as

$$\tau = \frac{60}{\Omega N_t} \text{ (sec)} \quad (4)$$

where  $\Omega$  is the spindle speed in rpm, and  $N_t$  is the number of teeth. The vibration in the direction of the surface normal for the current tooth depends on the  $x$  and  $y$  vibrations as well as the tooth angle according to

$$n = x \sin(\phi) - y \cos(\phi) \quad (5)$$

For the simulation, the strategy is to divide the angle of the cut into a discrete number of steps. At each small time step,  $dt$ , the cutter angle is incremented by the corresponding small angle,  $d$ . This approach enables convenient computation of the chip thickness for each simulation step because: (1) the possible teeth orientations are predefined and (2) the surface created by the previous teeth at each angle may be stored. The cutter rotation

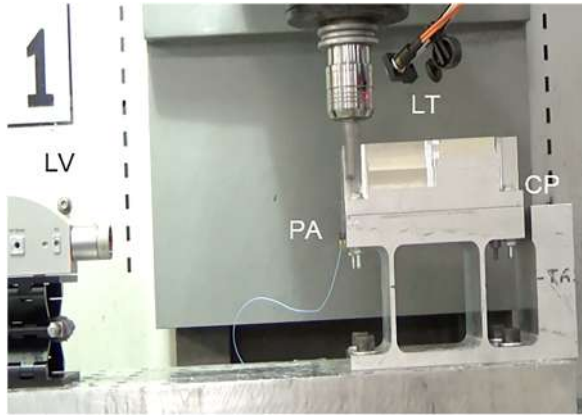


Fig. 2 Milling experimental setup with laser vibrometer (LV), piezo-accelerometer (PA), laser tachometer (LT), and capacitance probe (CP)

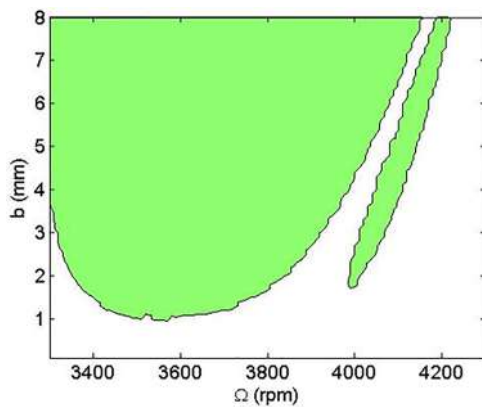


Fig. 3 Simulated stability map for experimental setup ( $M = 1 \mu\text{m}$  contour)

$$d\phi = \frac{360}{\text{SR}} (\text{deg}) \quad (6)$$

depends on the selection of the number of steps per revolution, SR. The corresponding time step is

$$dt = \frac{60}{\text{SR} \cdot \Omega} (\text{sec}) \quad (7)$$

A vector of angles is defined to represent the potential orientations of the teeth as the cutter is rotated through one revolution of the

circular tool path,  $\phi = [0, d\phi, 2d\phi, 3d\phi, \dots, (\text{SR} - 1)d\phi]$ . The locations of the teeth within the cut are then defined by referencing entries in this vector.

In order to accommodate the helix angle for the tool's cutting edges, the tool may be sectioned into a number of axial slices. Each slice is treated as an individual straight tooth endmill, where the thickness of each slice is a small fraction,  $db$ , of the axial depth of cut,  $b$ . Each slice incorporates a distance delay

$$r\chi = db \tan(\gamma) \quad (8)$$

relative to the prior slice (nearer the cutter free end), which becomes the angular delay between slices

$$\chi = \frac{db \tan(\gamma)}{r} = \frac{2db \tan(\gamma)}{d} (\text{rad}) \quad (9)$$

for the rotating endmill, where  $d$  is the endmill diameter, and  $\gamma$  is the helix angle. In order to ensure that the angles for each axial slice match the predefined tooth angles, the delay angle between slices is

$$\chi = d\phi \quad (10)$$

This places a constraint on the  $db$  value. By substituting  $d$  for  $\chi$  and rearranging, the required slice width is

$$db = \frac{d \cdot d\phi}{2 \tan(\gamma)} \quad (11)$$

This simple description can be extended to include:

- (1) Multiple tool modes—the  $x$  and  $y$  forces are used to calculate the acceleration, velocity, and displacement for each tool mode (represented by the modal parameters), and the results are summed in each direction.
- (2) Flexible workpiece—the  $x$  and  $y$  forces are also used to determine the workpiece deflections, again by numerical integration, and the relative tool–workpiece vibration is used to calculate the instantaneous chip thickness.
- (3) Runout of the cutter teeth—the chip thickness is updated by the runout of the current tooth.
- (4) Unequal teeth spacing—the tooth angle vector is modified to account for the actual tooth pitch.

**Stability Metric.** To construct a stability map using time-domain simulation, a separate simulation is completed at each position in the desired grid of spindle speed and axial depth values. A primary challenge in this approach, however, is automatically establishing the stability limit using the predicted time-domain signals. As described in Ref. [1], a new stability criterion

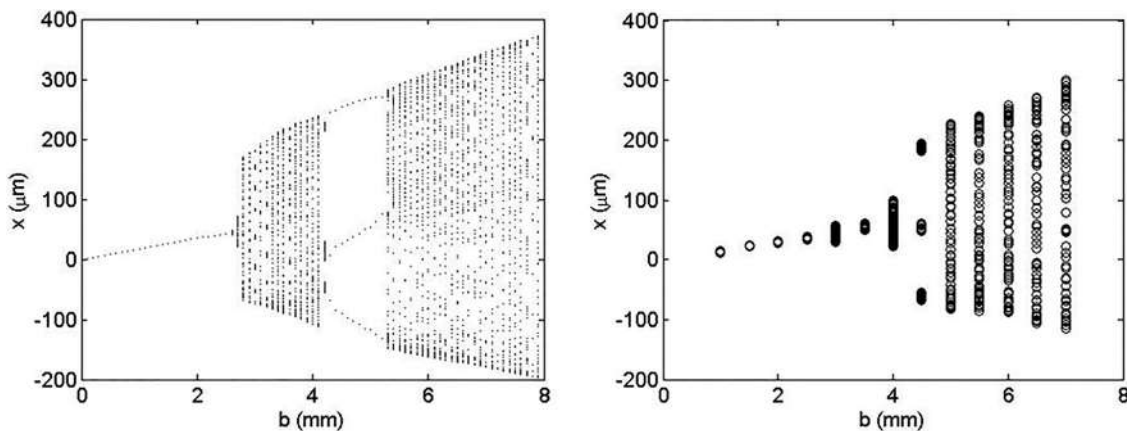


Fig. 4 Bifurcation diagram for 3800 rpm, 26% radial immersion (left) simulated and (right) experiment



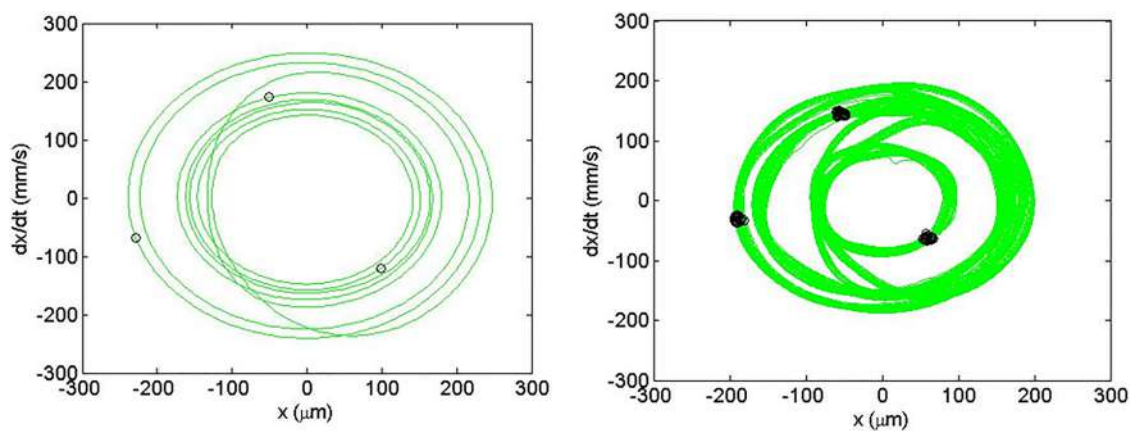


Fig. 5 Poincaré maps for 3800 rpm, 4.5 mm axial depth (left) simulated and (right) experiment

based on the once per tooth sampled data may be implemented. The new stability metric is

$$M1 = \frac{\sum_{i=2}^N |x_{s1}(i) - x_{s1}(i-1)|}{N} \quad (12)$$

where  $x_{s1}$  is the vector of once per tooth sampled  $x$  displacements, and  $N$  is the length of the  $x_{s1}$  vector. Other variables such as  $y$  displacement or cutting force could be selected as well. With this new stability metric, the absolute value of the differences in the

successive sampled points is summed and then normalized. The sampled points repeat for a stable cut, so the  $M1$  value is ideally zero. For unstable cuts, on the other hand,  $M1 > 0$ , due to the asynchronous motion in secondary Hopf instability and jumps from one fixed point to the next in period- $n$  bifurcations.

Example results are presented here. The flexure-based setup displayed in Fig. 2 was used to define a physical system for simulation and testing [1]. The setup included a parallelogram leaf-type flexure with an aluminum workpiece mounted on top [32]. The in-process vibration data were collected using a laser vibrometer (velocity) and capacitance probe (displacement). Once per

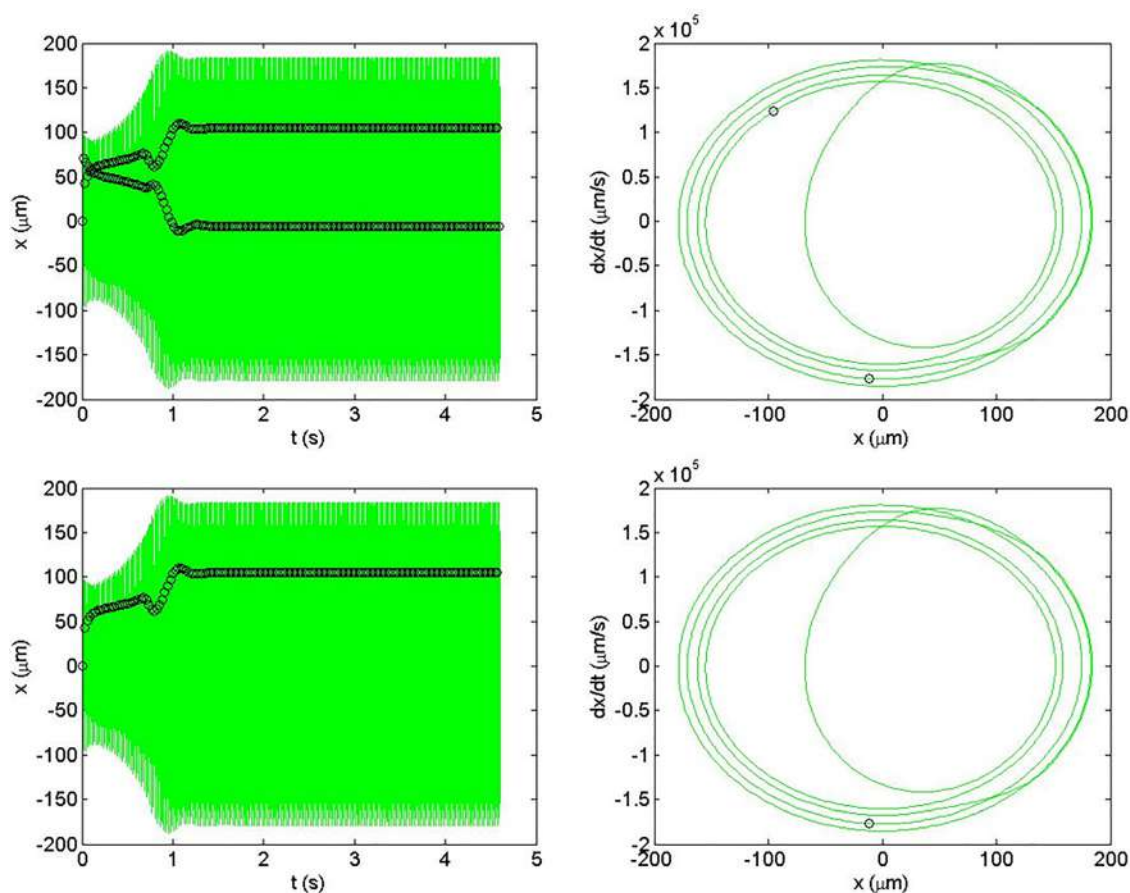
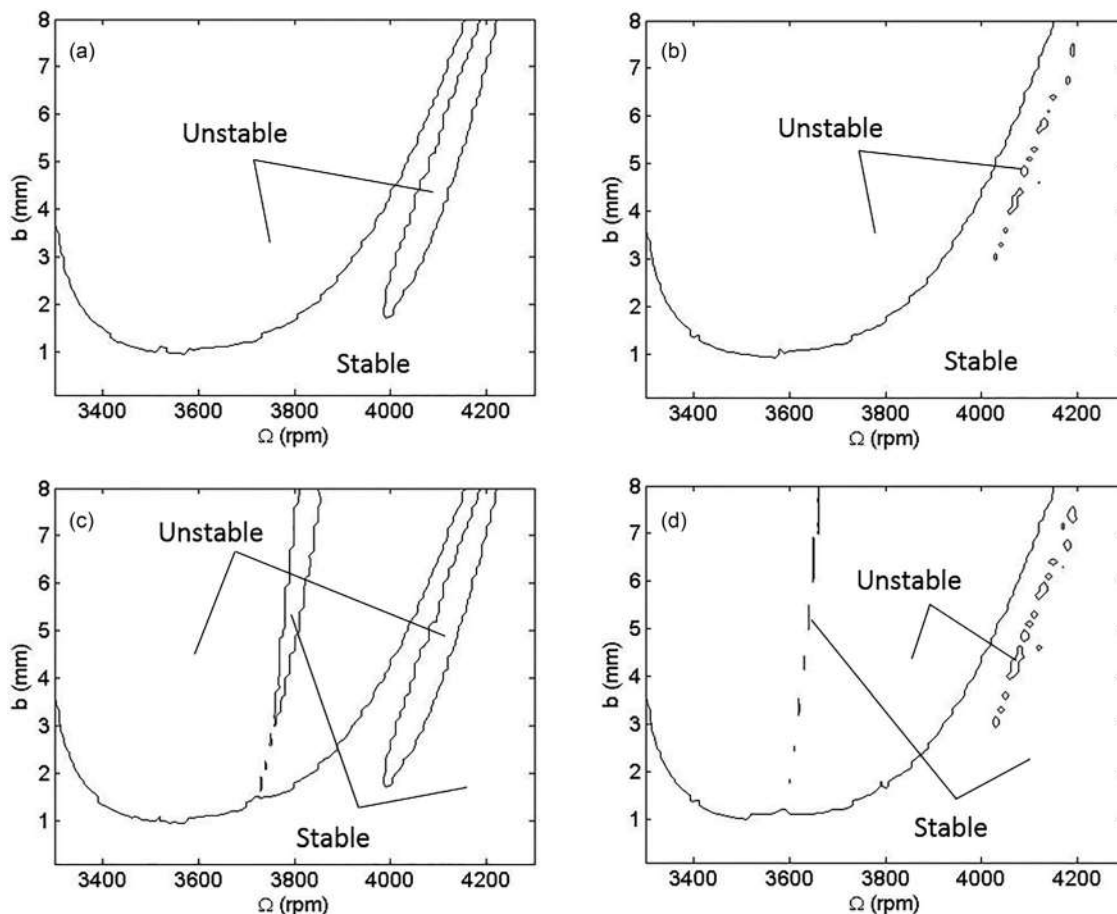


Fig. 6 Simulation results for a spindle speed of 4070 rpm at an axial depth of 3.6 mm. The workpiece  $x$  and  $y$  displacements are shown. (Top row) Time history (left) and Poincaré map (right) for once per tooth sampling ( $\tau$  sampling period). (Bottom row) Time history (left) and Poincaré map (right) for subharmonic sampling at  $2\tau$ .



**Fig. 7** (a) Once per tooth sampling ( $\tau$  sampling period), (b)  $2\tau$  sampling period, (c)  $3\tau$  sampling period, and (d)  $4\tau$  sampling period. The zones that appear to be stable and unstable, depending on the sampling period, are marked.

tooth sampling was accomplished using a laser tachometer and reflective target attached to the rotating tool holder. Acceleration was also measured using a piezoelectric accelerometer. The flexure dynamics were identified by modal testing: 163 Hz natural frequency, 0.007 viscous damping ratio, and  $5.2 \times 10^6$  N/m stiffness in the flexible (feed) direction. The dynamics for the 19.1 mm diameter, 30 deg helix angle tool (one tooth) were symmetric: 1050 Hz natural frequency, 0.045 viscous damping ratio, and  $3.85 \times 10^7$  N/m stiffness. The aluminum alloy cutting force coefficients were:  $k_{tc} = 792 \times 10^6$  N/m<sup>2</sup>,  $k_{nc} = 392 \times 10^6$  N/m<sup>2</sup>,  $k_{te} = 26 \times 10^3$  N/m, and  $k_{ne} = 28 \times 10^3$  N/m.

A simulated stability map for up milling with a radial depth of 5 mm (26% radial immersion) and 0.15 mm feed per tooth was generated for axial depths of cut from 0.1 mm to 8 mm in steps of 0.1 mm and spindle speeds from 3300 rpm to 4300 rpm in steps of 10 rpm. See Fig. 3, where the initial transients were removed prior to analysis using Eq. (12) (i.e., the final 75 tooth periods of a 750 tooth period simulation were analyzed). A single filled contour at  $M1 = 1 \mu\text{m}$  is displayed to distinguish between stable (white zone below the contour) and unstable (dark zone above the contour) conditions. An unstable “island” is seen starting at approximately 4000 rpm within the large stable zone.

A bifurcation diagram, which plots the sampled points versus the variable of interest (axial depth in this case), for a spindle speed of 3800 rpm was also predicted by simulation, and then, validation cuts were performed from 1 mm to 7 mm axial depths in 0.5 mm steps. The capacitance probe displacement signal from the experiments was sampled using the laser tachometer to construct an experimental bifurcation diagram. Figure 4 provides the comparison between prediction and experiment. The transition from

stable to secondary Hopf to period-3 to secondary Hopf is seen in both the simulation and experiment. Figure 5 shows the simulated and experimental Poincaré maps ( $x$  displacement versus velocity trajectory with once per tooth sampled points) for an axial depth of 4.5 mm at the same spindle speed. Good agreement is observed for the period-3 bifurcation.

**Subharmonic Sampling Strategy.** Periodic sampling at the tooth period,  $\tau$ , enables stable and unstable zones to be identified, but this approach does not distinguish between secondary Hopf and period- $n$  instabilities. As shown in Fig. 3, the unstable zone is identified, but the different types of instabilities of are not. For example, from Fig. 4 it is known that both secondary Hopf and period-3 bifurcations are present at 3800 rpm, but both simply appear in the unstable zone in Fig. 3. However, using subharmonic sampling at  $n\tau$  ( $n = 2, 3, 4, \dots$ ), the corresponding period- $n$  bifurcations can be separately established. For example, when sampling at  $2\tau$ , the stability metric becomes “blind” to period-2 bifurcations. By sampling at every other tooth passage ( $2\tau$ ), the period-2 behavior appears as synchronous motion (stable). The same is true for period-3 bifurcations if the sampling interval is  $3\tau$ , and so on.

Considering the same flexure-based dynamic system, a simulation was performed for a spindle speed of 4070 rpm at an axial depth of 3.6 mm. This is within the unstable island in Fig. 3. The time history and Poincaré map are displayed in the top row of Fig. 6 for once per tooth sampling. A period-2 bifurcation is observed. The  $M1$  value is  $106.7 \mu\text{m}$  for the period-2 instability; this value was calculated from the flexure (workpiece)  $x$  direction

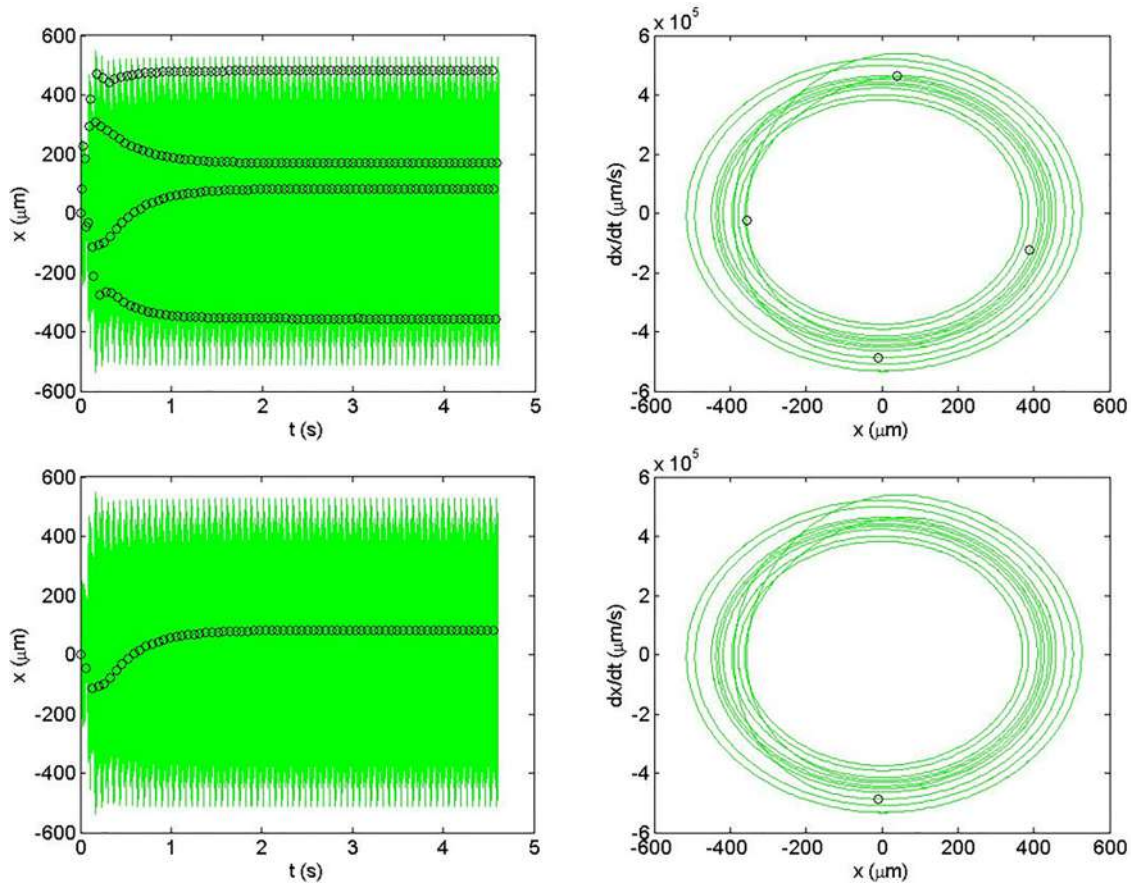


**Fig. 8** Simulation results for a spindle speed of 4070 rpm at an axial depth of 3.6 mm. The workpiece  $x$  and  $y$  displacements are shown. (Top row) Time history (left) and Poincaré map (right) for once per tooth sampling ( $\tau$  sampling period). (Bottom row) Time history (left) and Poincaré map (right) for subharmonic sampling at 4x.

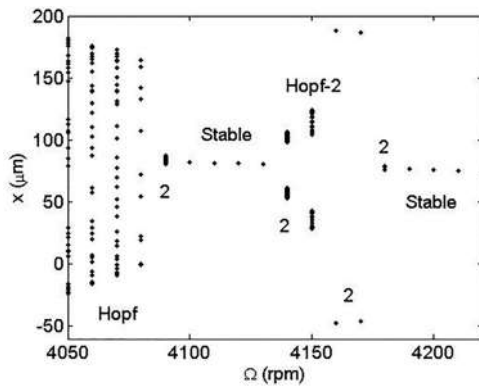


**Fig. 9** Bifurcation diagram for an axial depth of 6.4 mm. Hopf (Hopf), period-2 (2), stable (stable), and combination Hopf and period-2 (Hopf-2) behaviors are specified.

displacement for the final 75 tooth periods of a 750 tooth period simulation. The bottom row shows the results for  $2\tau$  subharmonic sampling. The metric for this case is

$$M2 = \frac{\sum_{i=2}^N |x_{s2}(i) - x_{s2}(i-1)|}{N} \quad (13)$$

where  $x_{s2}$  is the vector of  $x$  displacements sampled once every other tooth period (i.e., a  $2\tau$  sampling period), and  $N$  is the length

of the  $x_{s2}$  vector. It is observed that the cut now appears to be stable; the  $M2$  value is  $1.2 \times 10^{-9} \mu\text{m} \cong 0$ . Generically, the metric can be expressed as shown in Eq. (14), where the integer  $n = 1, 2, 3, \dots$  defines the sampling period (i.e.,  $n\tau$ )

$$Mn = \frac{\sum_{i=2}^N |x_{sn}(i) - x_{sn}(i-1)|}{N} \quad (14)$$

Next, the stability map shown in Fig. 3 was developed using  $n\tau$  sampling with  $n = 1, 2, 3$ , and 4. These results are provided in Fig. 7. In Fig. 7(a), once per tooth sampling ( $\tau$  sampling period) was applied to calculate  $M1$  using Eq. (12). A single contour is plotted at  $M1 = 1 \mu\text{m}$ . For Fig. 7(b), the sampling period is  $2\tau$ . It is seen that the unstable island no longer appears. This follows from Fig. 6, where it is seen that the  $2\tau$  sampling is blind to period-2 bifurcations. A single contour is plotted at  $M2 = 1 \mu\text{m}$  according to Eq. (13). In Fig. 7(c),  $3\tau$  sampling is applied. The period-2 bifurcation zone reappears as shown in Fig. 7(a), but a new “stable” zone is also visible. This is the region of period-3 bifurcations that is demonstrated in Figs. 4 and 5, but was not previously visible with the once per tooth sampling approach. Figure 7(d) displays the results for  $4\tau$  sampling. The period-2 bifurcations are again eliminated because  $2\tau$  is a factor of  $4\tau$ . However, a new stable band also appears to the left of the period-3 bifurcation zone in Fig. 7(c). This new band identifies period-4 bifurcations and would not have been discovered without subharmonic sampling. In Figs. 7(c) and 7(d), the stability metric (Eqs. (12) and (13)) was updated to accommodate the new sampling periods, and a single contour at a metric value of  $1 \mu\text{m}$  was plotted.



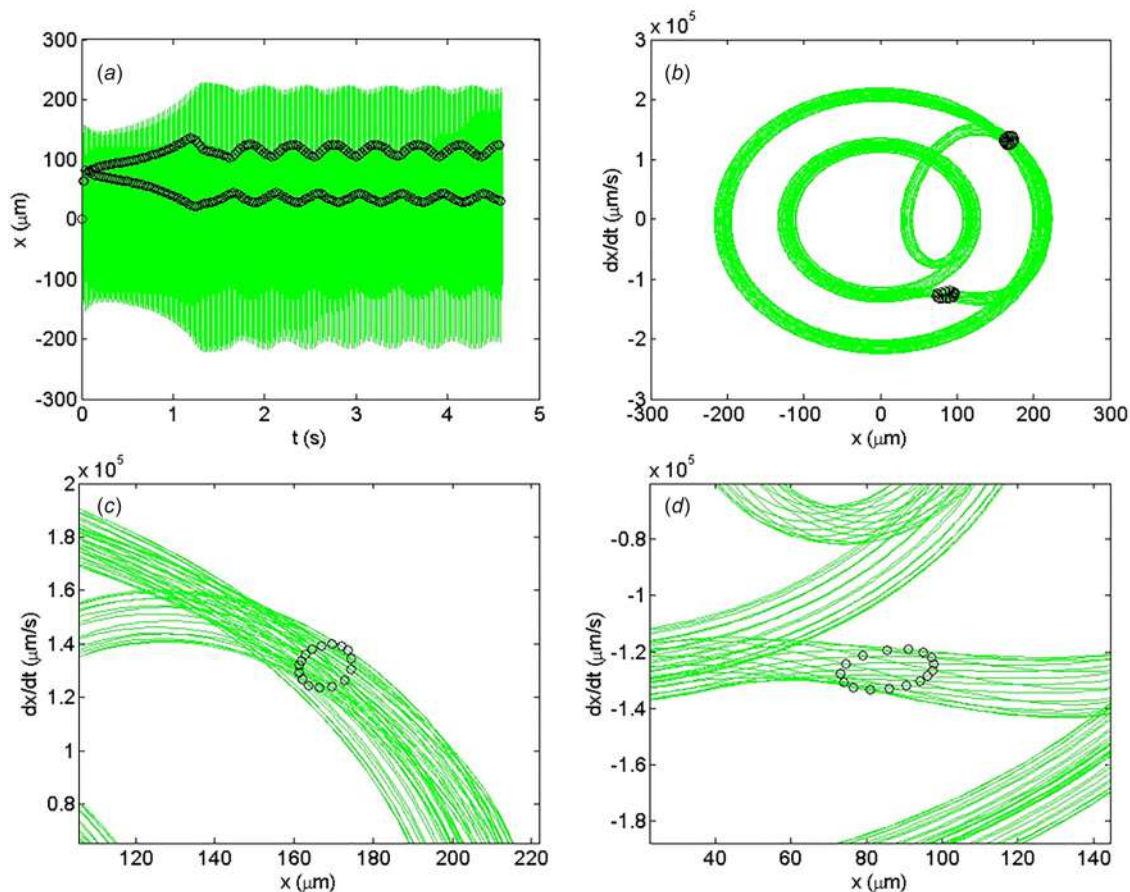


Fig. 10 Simulation results for a spindle speed of 4150 rpm at an axial depth of 6.4 mm. The workpiece  $x$  and  $y$  displacements are shown. (Top row) Time history (left) and Poincaré map (right) for once per tooth sampling. (Bottom row) Higher magnification views of the two elliptical distributions of once per tooth sampled points.

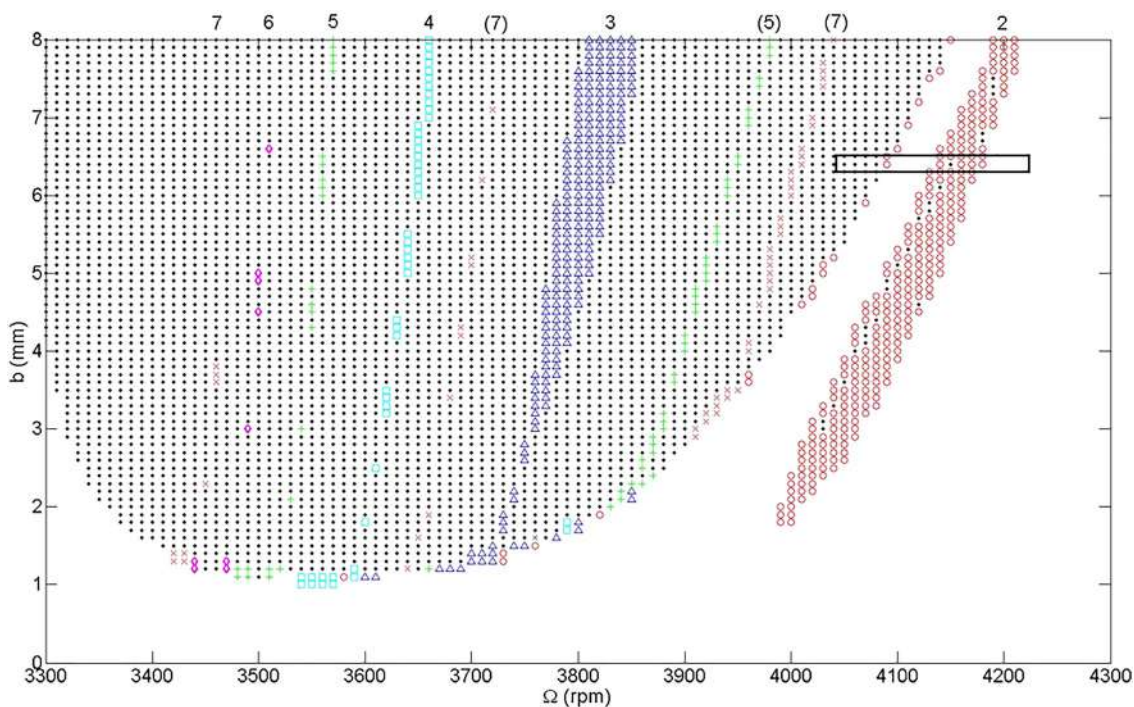


Fig. 11 New stability map. Period-2 (circle), period-3 (triangle), period-4 (square), period-5 (+), period-6 (diamond), period-7 (×), and secondary Hopf (dot) bifurcations are individually identified. The box indicates the spindle speed range and axial depth (6.4 mm) for the bifurcation diagram in Fig. 9.

To illustrate the period-4 bifurcations in Fig. 7(d), a simulation was completed at 3640 rpm with an axial depth of 5.3 mm. The time history and Poincaré map for both  $\tau$  and  $4\tau$  sampling periods are displayed in Fig. 8. The period-4 behavior is seen.

Figures 7(b) and 7(d) show the residual content where the period-2 bifurcations were previously present prior to the  $2\tau$  sampling. To explore these remaining unstable zones, a bifurcation diagram was generated at an axial depth of 6.4 mm for spindle speeds from 3950 rpm to 4150 rpm. This spindle speed range transitions from the unstable zone, to the stable zone, through the residual unstable point, to the period-2 bifurcations, and finally back to the stable zone (to the right of the period-2 island). The diagram is shown in Fig. 9, and the various behaviors are identified.

The combination secondary Hopf/period-2 behavior (labeled Hopf-2) is the reason for the residual unstable zones in Figs. 7(b) and 7(d). This quasi-periodic instability is shown in Fig. 10, which displays the time history and Poincaré map for a spindle speed of 4150 rpm, where two separate ellipses are observed. The elliptical distribution of once per tooth sampled points is characteristic of secondary Hopf bifurcations; two ellipses indicate the simultaneous presence of period-2 behavior.

## New Stability Map

The subharmonic sampling approach is now implemented to construct a stability map that individually identifies each bifurcation type. The metrics  $M1 - M7$ , which represent  $\tau - 7\tau$  integer sampling periods, are used to isolate the stable zone as well as the different bifurcation types: period-2, -3, -4, -5, -6, -7, and secondary Hopf. The logic used to construct the stability map is as follows:

---

```

if  $M1 \leq 1 \mu\text{m}$ 
    (stable, do nothing)
elseif  $M2 \leq 1 \mu\text{m}$ 
    plot a circle (period-2)
elseif  $M3 \leq 1 \mu\text{m}$ 
    plot a triangle (period-3)
elseif  $M4 \leq 1 \mu\text{m}$  and  $M2 > 1 \mu\text{m}$ 
    plot a square (period-4, excludes period-2)
elseif  $M5 \leq 1 \mu\text{m}$ 
    plot a + (period-5)
elseif  $M6 \leq 1 \mu\text{m}$  and  $M2 > 1 \mu\text{m}$  and  $M3 > 1 \mu\text{m}$ 
    plot a diamond (period-6, excludes period-2 and period-3)
elseif  $M7 \leq 1 \mu\text{m}$ 
    plot an  $\times$  (period-7)
else
    plot a dot (secondary Hopf or high order period- $n$ )
end

```

---

The result is displayed in Fig. 11. The stable zone is the open white area, and the various instabilities are indicated by the symbols. Note that the behavior shown in Figs. 9 and 10 is captured in the map at an axial depth of 6.4 mm. The single unstable point within the period-2 zone is seen. The box in the figure indicates the spindle speed range and axial depth (6.4 mm) for the bifurcation diagram in Fig. 9.

By following the bifurcations in the map from period-2 (circle), to -3 (triangle), to -4 (square), to -5 (+), to -6 (diamond), and to -7 ( $\times$ ), it appears that a pattern is emerging. Within the single stability lobe, the increasing order shifts the period- $n$  zones to progressively lower spindle speeds. Also, the size of the zones diminishes with increasing order. The period numbers for the various zones are provided above the stability map in Fig. 11. For period-5 and -7 bifurcations, there are additional zones that appear to “fold over” to higher speeds; these are denoted by parenthetical order numbers in Fig. 11. There is one of these fold over zones for period-5 and two for period-7. This interesting behavior suggests a focus area for follow-on studies.

## Conclusions

This paper described the use of (periodic) subharmonic sampling to distinguish between secondary Hopf and period- $n$

bifurcations in milling. Background information on milling stability prediction, with an emphasis on period- $n$  bifurcations, was presented. A time-domain simulation was then detailed, and the application of subharmonic sampling to time-domain results and identification of period- $n$  bifurcations was demonstrated. A new stability map based on the subharmonic sampling was finally shown. This work presents a new approach to the automatic identification of instability types and its inclusion in a comprehensive stability map for milling.

## Acknowledgment

This material was based on the work supported by the National Science Foundation under Grant No. CMMI-1561221.

## References

- [1] Honeycutt, A., and Schmitz, T., 2016, “A New Metric for Automated Stability Identification in Time Domain Milling Simulation,” *ASME J. Manuf. Sci. Eng.*, **138**(7), p. 074501.
- [2] Arnold, R. N., 1946, “The Mechanism of Tool Vibration in the Cutting of Steel,” *Proc. Inst. Mech. Eng.*, **154**(1), pp. 261–284.
- [3] Doi, S., and Kato, S., 1956, “Chatter Vibration of Lathe Tools,” *Trans. ASME*, **78**(5), pp. 1127–1134.
- [4] Tobias, S. A., and Fishwick, W., 1958, “The Chatter of Lathe Tools Under Orthogonal Cutting Conditions,” *Trans. ASME*, **80**(2), pp. 1079–1088.
- [5] Tlustý, J., and Polacek, M., 1963, “The Stability of Machine Tools Against Self-Excited Vibrations in Machining,” *Intl. Res. Prod. Eng.*, **1**(1), pp. 465–474.
- [6] Tobias, S. A., 1965, *Machine Tool Vibration*, Wiley, New York.
- [7] Merritt, H. E., 1965, “Theory of Self-Excited Machine-Tool Chatter,” *ASME J. Eng. Ind.*, **87**(4), pp. 447–454.
- [8] Tlustý, J., and Polacek, M., 1968, “Experience With Analysing Stability of Machine Tool Against Chatter,” 9th MTDR Conference, pp. 521–570.
- [9] Shridar, R., Hohn, R. E., and Long, G. W., 1968, “A General Formulation of the Milling Process Equation,” *ASME J. Eng. Ind.*, **90**(2), pp. 317–324.
- [10] Hohn, R. E., Shridar, R., and Long, G. W., 1968, “A Stability Algorithm for a Special Case of the Milling Process,” *ASME J. Eng. Ind.*, **90**(2), pp. 326–329.
- [11] Shridar, R., Hohn, R. E., and Long, G. W., 1968, “A Stability Algorithm for the General Milling Process,” *ASME J. Eng. Ind.*, **90**(2), pp. 330–334.
- [12] Hanna, N. H., and Tobias, S. A., 1974, “A Theory of Nonlinear Regenerative Chatter,” *ASME J. Eng. Ind.*, **96**(1), pp. 247–255.
- [13] Tlustý, J., and Ismail, F., 1981, “Basic Non-Linearity in Machining Chatter,” *Ann. CIRP*, **30**(1), pp. 299–304.
- [14] Tlustý, J., and Ismail, F., 1983, “Special Aspects of Chatter in Milling,” *ASME J. Vib. Stress Reliab. Des.*, **105**(1), pp. 24–32.
- [15] Tlustý, J., 1985, “Machine Dynamics,” *Handbook of High-Speed Machining Technology*, R. I. King, ed., Chapman and Hall, New York, pp. 48–153.
- [16] Tlustý, J., 1986, “Dynamics of High-Speed Milling,” *ASME J. Eng. Ind.*, **108**(2), pp. 59–67.
- [17] Minis, I., and Yanusevsky, R., 1993, “A New Theoretical Approach for Prediction of Chatter in Milling,” *ASME J. Eng. Ind.*, **115**(1), pp. 1–8.
- [18] Altintas, Y., and Budak, E., 1995, “Analytical Prediction of Stability Lobes in Milling,” *Ann. CIRP*, **44**(1), pp. 357–362.
- [19] Davies, M. A., Dutterer, B. S., Pratt, J. R., and Schaut, A. J., 1998, “On the Dynamics of High-Speed Milling With Long, Slender Endmills,” *Ann. CIRP*, **47**(1), pp. 55–60.
- [20] Moon, F. C., and Kalmár-Nagy, T., 2001, “Nonlinear Models for Complex Dynamics in Cutting Materials,” *Philos. Trans. R. Soc. London A*, **359**(1781), pp. 695–711.
- [21] Davies, M. A., Pratt, J. R., Dutterer, B. S., and Burns, T. J., 2000, “The Stability of Low Radial Immersion Milling,” *Ann. CIRP*, **49**(1), pp. 37–40.
- [22] Moon, F. C., 1994, “Chaotic Dynamics and Fractals in Material Removal Processes,” *Nonlinearity and Chaos in Engineering Dynamics*, J. Thompson and S. Bishop, eds., Wiley, Hoboken, NJ, pp. 25–37.
- [23] Bukkapatnam, S., Lakhtakia, A., and Kumara, S., 1995, “Analysis of Sensor Signals Shows Turning on a Lathe Exhibits Low-Dimensional Chaos,” *Phys. Rev. E*, **52**(3), pp. 2375–2387.
- [24] Stépán, G., and Kalmár-Nagy, T., 1997, “Nonlinear Regenerative Machine Tool Vibrations,” *ASME Paper No. DETC 97/VIB-4021*.
- [25] Nayfeh, A., Chin, C., and Pratt, J., 1998, “Applications of Perturbation Methods to Tool Chatter Dynamics,” *Dynamics and Chaos in Manufacturing Processes*, F. C. Moon, ed., Wiley, Hoboken, NJ, pp. 193–213.
- [26] Minis, I., and Berger, B. S., 1998, “Modelling, Analysis, and Characterization of Machining Dynamics,” *Dynamics and Chaos in Manufacturing Processes*, F. C. Moon, ed., Wiley, Hoboken, NJ, pp. 125–163.
- [27] Moon, F. C., and Johnson, M., 1998, “Nonlinear Dynamics and Chaos in Manufacturing Processes,” *Dynamics and Chaos in Manufacturing Processes*, F. C. Moon, ed., Wiley, Hoboken, NJ, pp. 3–32.
- [28] Smith, K. S., and Tlustý, J., 1991, “An Overview of Modeling and Simulation of the Milling Process,” *ASME J. Eng. Ind.*, **113**(2), pp. 169–175.



- [29] Campomanes, M. L., and Altintas, Y., 2003, "An Improved Time Domain Simulation for Dynamic Milling at Small Radial Immersions," *ASME J. Manuf. Sci. Eng.*, **125**(3), pp. 416–422.
- [30] Zhao, M. X., and Balachandran, B., 2001, "Dynamics and Stability of Milling Process," *Int. J. Solids Struct.*, **38**(10–13), pp. 2233–2248.
- [31] Davies, M. A., Pratt, J. R., Dutterer, B., and Burns, T. J., 2002, "Stability Prediction for Low Radial Immersion Milling," *ASME J. Manuf. Sci. Eng.*, **124**(2), pp. 217–225.
- [32] Mann, B. P., Insperger, T., Bayly, P. V., and Stépán, G., 2003, "Stability of Up-Milling and Down-Milling—Part 2: Experimental Verification," *Int. J. Mach. Tools Manuf.*, **43**(1), pp. 35–40.
- [33] Mann, B. P., Insperger, T., Bayly, P. V., and Stépán, G., 2003, "Stability of Up-Milling and Down-Milling—Part 1: Alternative Analytical Methods," *Int. J. Mach. Tools Manuf.*, **43**(1), pp. 25–34.
- [34] Insperger, T., Stépán, G., Bayly, P. V., and Mann, B. P., 2003, "Multiple Chatter Frequencies in Milling Processes," *J. Sound Vib.*, **262**(2), pp. 333–345.
- [35] Insperger, T., and Stépán, G., 2004, "Vibration Frequencies in High-Speed Milling Processes or a Positive Answer to Davies, Pratt, Dutterer, and Burns," *ASME J. Manuf. Sci. Eng.*, **126**(3), pp. 481–487.
- [36] Mann, B. P., Bayly, P. V., Davies, M. A., and Halley, J. E., 2004, "Limit Cycles, Bifurcations, and Accuracy of the Milling Process," *J. Sound Vib.*, **277**(1–2), pp. 31–48.
- [37] Merdol, S. D., and Altintas, Y., 2004, "Multi Frequency Solution of Chatter Stability for Low Immersion Milling," *ASME J. Manuf. Sci. Eng.*, **126**(3), pp. 459–466.
- [38] Govekar, E., Gradišek, J., Kalveram, M., Insperger, T., Weinert, K., Stepan, G., and Grabec, I., 2005, "On Stability and Dynamics of Milling at Small Radial Immersion," *Ann. CIRP*, **54**(1), pp. 357–362.
- [39] Gradišek, J., Kalveram, M., Insperger, T., Weinert, K., Stépán, G., Govekar, E., and Grabec, I., 2005, "On Stability Prediction for Milling," *Int. J. Mach. Tools Manuf.*, **45**(7–8), pp. 769–781.
- [40] Mann, B. P., Garg, N. K., Young, K. A., and Helvey, A. M., 2005, "Milling Bifurcations From Structural Asymmetry and Nonlinear Regeneration," *Nonlinear Dyn.*, **42**(4), pp. 319–337.
- [41] Stépán, G., Szalai, R., Mann, B. P., Bayly, P. V., Insperger, T., Gradišek, J., and Govekar, E., 2005, "Nonlinear Dynamics of High-Speed Milling—Analyses, Numerics, and Experiments," *ASME J. Vib. Acoust.*, **127**(2), pp. 197–203.
- [42] Zatarain, M., Muñoz, J., Peigné, G., and Insperger, T., 2006, "Analysis of the Influence of Mill Helix Angle on Chatter Stability," *Ann. CIRP*, **55**(1), pp. 365–368.
- [43] Insperger, T., Muñoz, J., Zatarain, M. A., and Peigné, G., 2006, "Unstable Islands in the Stability Chart of Milling Processes Due to the Helix Angle," *CIRP 2nd International Conference on High Performance Cutting*, Vancouver, Canada, pp. 12–13.
- [44] Patel, B. R., Mann, B. P., and Young, K. A., 2008, "Uncharted Islands of Chatter Instability in Milling," *Int. J. Mach. Tools Manuf.*, **48**(1), pp. 124–134.
- [45] Moradi, H., Vossoughi, G., and Movahhedy, M., 2014, "Bifurcation Analysis of Nonlinear Milling Process With Tool Wear and Process Damping: Sub-Harmonic Resonance Under Regenerative Chatter," *Int. J. Mech. Sci.*, **85**, pp. 1–19.
- [46] Honeycutt, A., and Schmitz, T., 2015, "The Extended Milling Bifurcation Diagram," *Procedia Manuf.*, **1**, pp. 466–476.
- [47] Honeycutt, A., and Schmitz, T., 2016, "A Numerical and Experimental Investigation of Period- $n$  Bifurcations in Milling," *ASME J. Manuf. Sci. Eng.*, **139**(1), p. 011003.
- [48] Schmitz, T., and Smith, K. S., 2009, *Machining Dynamics: Frequency Response to Improved Productivity*, Springer, New York.